Journal of Solid State Chemistry 184 (2011) 296–303

Contents lists available at ScienceDirect

Journal of Solid State Chemistry

journal homepage: www.elsevier.com/locate/jssc

High-pressure high-temperature synthesis and crystal structure of the isotypic rare earth (*RE*)–thioborate–sulfides $RE_9[BS_3]_2[BS_4]_3S_3$, (*RE*=Dy–Lu)

Marija Borna [a], Jens Hunger [a], Alim Ormeci [a], Dirk Zahn [b], Ulrich Burkhardt [a], Wilder Carrillo-Cabrera [a], Raul Cardoso-Gil [a], Rüdiger Kniep [a,*]

[a] Max Planck Institute for Chemical Physics of Solids, Nöthnitzer Strasse 40, D-01187 Dresden, Germany
[b] Computer-Chemie-Centrum, Friedrich-Alexander-Universität Erlangen-Nürnberg, Nägelsbach Strasse 25, D-91052 Erlangen, Germany

ARTICLE INFO

Article history:
Received 17 September 2010
Received in revised form
1 November 2010
Accepted 7 November 2010
Available online 13 November 2010

Keywords:
Rare earth compounds
Thioborates
Crystal structure
Quantum mechanical calculations
XAS
Chemical bonding analysis

ABSTRACT

Application of high-pressure high-temperature conditions (3.5 GPa at 1673 K for 5 h) to mixtures of the elements (*RE*:B:S=1:3:6) yielded crystalline samples of the isotypic rare earth–thioborate–sulfides $RE_9[BS_3]_2[BS_4]_3S_3$, (*RE*=Dy–Lu), which crystallize in space group $P6_3$ ($Z=2/3$) and adopt the $Ce_6Al_{3.33}S_{14}$ structure type. The crystal structures were refined from X-ray powder diffraction data by applying the Rietveld method. Dy: $a=9.4044(2)$ Å, $c=5.8855(3)$ Å; Ho: $a=9.3703(1)$ Å, $c=5.8826(1)$ Å; Er: $a=9.3279(12)$ Å, $c=5.8793(8)$ Å; Tm: $a=9.2869(3)$ Å, $c=5.8781(3)$ Å; Yb: $a=9.2514(5)$ Å, $c=5.8805(6)$ Å; Lu: $a=9.2162(3)$ Å, $c=5.8911(3)$ Å. The crystal structure is characterized by the presence of two isolated complex ions $[BS_3]^{3-}$ and $[BS_4]^{5-}$ as well as $[\square(S^{2-})_3]$ units.

1. Introduction

Well-defined boron compounds containing the heavier group 16 elements are fairly difficult to prepare due to the high reactivity of *in situ* formed boron chalcogenides towards most container materials at elevated temperatures. However, improvement and optimization of appropriate methods for syntheses and structural investigations provided considerable progress in the chemistry and the structural characterization of thio- and selenoborates [1].

Generally, high temperature reactions of the elements or the binary sulfides in closed systems mostly yield thioborates with either trigonal planar or tetrahedrally coordinated boron, as observed for several alkali, alkaline-earth and heavy metal compounds such as $M^{I}[BS_2]$, $M^{II}[B_2S_4]$, $M^{II}_4[B_4S_{10}]$, $M^{I}_3[BS_3]$, $M^{I}_2[B_2S_7]$ and $M^{I}_3[B_3S_6]$, as well as "perthioborates" $M^{I}_2[B_2S_5]$ and $M^{I}[BS_3]$ and the sulfur-deficient phases $M^{I}_8[B_{18}S_{18}]$, containing icosahedral boron clusters [2,3]. In this respect the ternary compound BaB_2S_4 [4] is an exception by containing both trigonal planar BS_3 and tetrahedral BS_4 groups which are connected *via* common corners resulting in infinite chains. The crystal structure of the until recently only known rare earth thioborate EuB_2S_4 [5] reveals polymeric $^{2}_{\infty}[(B_2S_4)^{2-}]$ units composed of BS_4 tetrahedra connected *via* common corners and edges. Recently, we discovered a new group of rare-earth orthothioborates $RE^{III}[BS_3]$ (*RE*=La–Nd, Sm, Gd, Tb) [6–11] containing trigonal planar $[BS_3]^{3-}$ units. While trigonal planar thioborate units tend to form rather simple monomers and oligomers, tetrahedral thioborate units are always connected to form larger complexes with often infinite extension. The smallest possible tetrahedral unit, an isolated $[BS_4]^{5-}$ species, has not been observed until now.

Here, we present a new series of isotypic *RE*–thioborate–sulfides with the general formula $RE_9B_5S_{21}$, (*RE*=Dy–Lu), obtained at high-pressure high-temperature (Hp–HT) conditions. Their crystal structures, determined from X-ray powder diffraction data, adopt the $Ce_6Al_{3.33}S_{14}$ structure type [12], containing both trigonal planar $[BS_3]^{3-}$ and tetrahedral $[BS_4]^{5-}$ units, as well as intrinsic vacancies. The vacancy distribution in the crystal structure of $Lu_9[BS_3]_2[BS_4]_3S_3$ was exemplary investigated by EXAFS, TEM and quantum mechanical calculations.

2. Materials and methods

2.1. Materials

The *RE* metals dysprosium (powder, ChemPur, 99.9%), holmium (powder, ChemPur, 99.9%), erbium (powder, ChemPur, 99.9%), thulium (powder, ChemPur, 99.9%), ytterbium (powder, ChemPur, 99.9%) and lutetium (powder, ChemPur, 99.9%), amorphous boron

* Corresponding author.
E-mail address: kniep@cpfs.mpg.de (R. Kniep).

0022-4596/$ - see front matter © 2010 Elsevier Inc. All rights reserved.
doi:10.1016/j.jssc.2010.11.004

(powder, ABCR, 99%) and sulfur (Alfa Aesar, 99.9995%) were the starting materials for all the reactions under investigation. *RE* metals and amorphous boron were used without further purification, while sulfur was sublimed under vacuum to reduce oxygen contamination below 1 wt%. All educts were controlled by means of elemental analysis using a LECO RH 404 analyzer (H), a LECO TC 436 DR/5 analyzer (N/O), a LECO C-200 CHLH analyzer (C) and a simultaneous inductively coupled plasma-optical emission (ICP-OES) Echelle spectrometer (other elements).

2.2. Synthesis

The ternary compounds with compositions $RE_9B_5S_{21}$, (*RE*=Dy–Lu) were prepared from mixtures of the respective *RE* metals, amorphous boron and sulfur in the molar ratio 1:3:6 by a high-pressure high-temperature (Hp–HT) synthetic route. Molar ratios corresponding to the chemical compositions of the compounds under investigation did not yield sufficiently pure materials. High-pressure conditions were achieved by using a hydraulic uniaxial press where force redistribution is accomplished by a Walker-type module and MgO octahedra with an edge length of 18 mm [13,14]. Elevated temperatures during the reactions were realized by resistive heating of graphite tubes enclosing the sample crucibles. Pressure and temperature calibration was performed prior to the experiments by monitoring the resistance changes of bismuth [15] and using a thermocouple, respectively. Sample handlings including loading of the high pressure setup were performed in a glove box operating with an argon atmosphere (MBraun, $H_2O < 1$ ppm; $O_2 < 1$ ppm). For the preparation of the *RE*–thioborate–sulfides, the octahedral assemblies for the Hp–HT syntheses were compressed to 3.5 GPa for 5 h and heated to 1673 K. Hexagonal boron nitride was used as the crucible material. After reaction, the central Hp–HT setup was removed from the press and transferred into a glove box where the sample was isolated from the crucible. No indications for reactions between the samples and the crucible material were observed. The air- and moisture-sensitive compounds $RE_9B_5S_{21}$, (*RE*=Dy–Lu; red-brown, red, dark orange, light orange, yellow, and yellow, respectively) were obtained as polycrystalline products. The erbium compound, however, was not obtained as a single phase sample. The minority phase present in this sample is not identified until now. Amorphous boron sulfide is present in all the reaction products. Our efforts to separate boron sulfide from the main reaction products by sublimation in vacuum at low temperatures remained hitherto unsuccessful.

2.3. X-ray crystallography

The unit cell parameters at ambient temperature (Table 1) were determined from X-ray powder diffraction data employing a HUBER G670 imaging-plate Guinier camera equipped with a Ge monochromator and Cu$K\alpha_1$ radiation (λ=1.54056 Å). LaB_6 (a=4.15692(1) Å) was used as internal standard. The unit cell parameters were refined by Le Bail fits [16] in the range $10^\circ \le 2\theta \le 100^\circ$ using the program suite WinCSD [17].

The crystal structures of $RE_9B_5S_{21}$, (*RE*=Dy–Lu) were refined from X-ray powder diffraction data collected on a STOE StadiP-MP diffractometer in Debye–Scherrer geometry equipped with a Ge(111) monochromator (Cu$K\alpha_1$ radiation, angular range $10^\circ \le 2\theta \le 110^\circ$ for *RE*=Dy–Yb and $10^\circ \le 2\theta \le 90^\circ$ for *RE*=Lu) [18]. The Rietveld refinement method [19] was applied by using the GSAS software package [20,21] (Fig. 1, Figs. S1 to S5 in the supporting information, Table 2, Table S1). The position of the

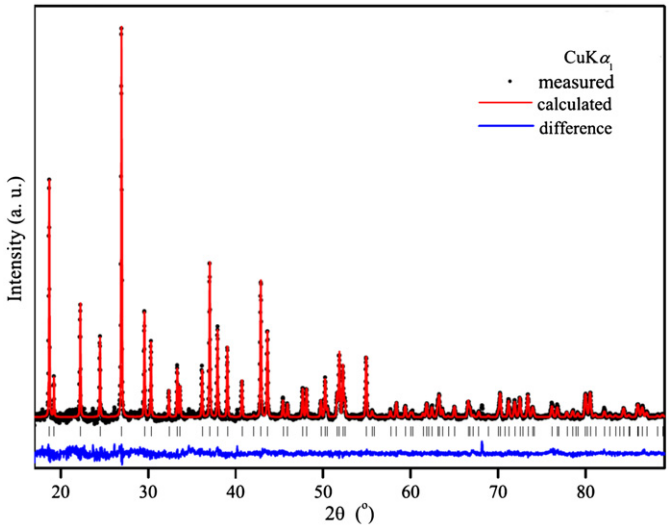

Fig. 1. X-ray powder diffraction patterns (measured and calculated from Rietveld refinements) of $Lu_9B_5S_{21}$.

Table 1
Crystallographic data and final *R* values from Rietveld refinements of the isotypic phases $RE_9B_5S_{21}$, (*RE*=Dy–Lu). Powder diffraction data were collected on a STOE StadiP-MP diffractometer using Cu$K\alpha_1$ (1.54056 Å) radiation at 298 K.

	$Dy_9B_5S_{21}$	$Ho_9B_5S_{21}$	$Er_9B_5S_{21}$	$Tm_9B_5S_{21}$	$Yb_9B_5S_{21}$	$Lu_9B_5S_{21}$
Color	Brown-red	Red	Dark orange	Light orange	Yellow	Yellow
Space group, *Z*	$P6_3$, 2/3	$P6_3$, 2/3	$P6_3$, 2/3	$P6_3$, 2/3	$P6_3$, 2/3	$P6_3$, 2/3
Formula mass (g mol^{-1})	2189.82	2211.69	2232.66	2247.72	2284.68	2302.02
a (Å) [a]	9.4044(2)	9.3703(1)	9.3279(12)	9.2869(3)	9.2514(5)	9.2162(3)
c (Å) [a]	5.8855(3)	5.8826(1)	5.8793(8)	5.8781(3)	5.8805(6)	5.8911(3)
Cell volume (Å^3) [a]	450.79(4)	447.31(1)	443.02(9)	439.03(3)	435.87(7)	433.34(4)
Density (g cm^{-3})	5.381	5.473	5.584	5.666	5.807	5.888
Weighted profile *R*-factor, R_{wp}	0.037	0.047	0.065	0.030	0.031	0.015
Profile *R*-factor, R_p	0.026	0.025	0.048	0.023	0.025	0.013
Structure *R*-factor, R_F	0.099	0.064	0.137	0.024	0.029	0.087
Expected *R*-factor, R_{exp}	0.024	0.014	0.017	0.013	0.016	0.012

Rietveld refinement was used to minimize $\sum w_i(I_{o,i}-I_{c,i})^2$, where $I_{o,i}$ and $I_{c,i}$ are the observed and calculated powder diffraction intensities for the *i*th point, respectively. Weights, w_i, are defined as $1/I_{o,i}$. Weighted and non weighted profile *R*-factors are defined as $R_{wp}=\sqrt{\sum_{wi}(I_{o,i}-I_{c,i})^2/\sum_{wi}(I_{o,i})^2}$ and $R_p=\sum|(I_{o,i}-I_{c,i})|/\sum I_{o,i}$. The structure factor R_F is defined as $R_F=\sum(F_o-F_c)^2/\sum(F_o)^2$. The expected R-factor (the statistically best possible value for R_{wp}) is defined as $R_{exp}=\sqrt{N-P/\sum w_i(I_{o,i})^2}$ where *N* is the number of observed powder diffraction data points and *P* is the number of refined parameters.

[a] Obtained from Le Bail fit.

Table 2
Fractional atomic coordinates and isotropic displacement parameters of the crystal structure of $RE_9B_5S_{21}$, (RE=Dy–Lu); estimated standard deviations are given in parentheses.

Atom	Site	x	y	z	U_{iso} (Å^2)
$Dy_9B_5S_{21}$					
Dy1	6*c*	0.3775(3)	0.1492(3)	0.3088(13)	0.0268(4)
S1	6*c*	0.2330(13)	0.0903(15)	0.8826(17)	0.0300(19)
S2	6*c*	0.5376(8)	0.4244(9)	0.6054(17)	0.0300
S3	2*b*	0.3333	0.6667	0.5602(12)	0.0300
B1	2*b*	0.3333	0.6667	0.2293(13)	0.0300
B2	2*a*	0.0	0.0	0.8826(17)	0.0300
$Ho_9B_5S_{21}$					
Ho1	6*c*	0.37830(12)	0.15062(12)	0.3161(8)	0.0239(2)
S1	6*c*	0.1371(6)	0.2341(4)	0.3867(9)	0.0154(7)
S2	6*c*	0.1130(5)	0.5279(6)	0.1139(9)	0.0154
S3	2*b*	0.3333	0.6667	0.5637(12)	0.0154
B1	2*b*	0.3333	0.6667	0.2364(21)	0.0154
B2	2*a*	0.0	0.0	0.3867(9)	0.0154
$Er_9B_5S_{21}$					
Er1	6*c*	0.37888(20)	0.15245(19)	0.3598(16)	0.0140(3)
S1	6*c*	0.1340(13)	0.2160(9)	0.2879(19)	0.0289(19)
S2	6*c*	0.1054(10)	0.5253(13)	0.1357(19)	0.029
S3	2*b*	0.3333	0.6667	0.5613(20)	0.029
B1	2*b*	0.3333	0.6667	0.2336(23)	0.029
B2	2*a*	0.0	0.0	0.2879(19)	0.029
$Tm_9B_5S_{21}$					
Tm1	6*c*	0.37831(10)	0.15160(10)	0.3144(7)	0.0192(2)
S1	6*c*	0.1367(6)	0.2323(4)	0.3977(8)	0.0126(9)
S2	6*c*	0.1109(5)	0.5354(6)	0.1099(9)	0.0126
S3	2*b*	0.3333	0.6667	0.5649(12)	0.0126
B1	2*b*	0.3333	0.6667	0.236(3)	0.0126
B2	2*a*	0.0	0.0	0.3977(8)	0.0126
$Yb_9B_5S_{21}$					
Yb1	6*c*	0.37889(6)	0.15252(5)	0.3040(4)	0.0186(1)
S1	6*c*	0.2325(3)	0.0967(4)	0.8890(5)	0.0155(1)
S2	6*c*	0.5350(4)	0.4252(3)	0.5976(6)	0.0155
S3	2*b*	0.3333	0.6667	0.5570(9)	0.0155
B1	2*b*	0.3333	0.6667	0.2283(23)	0.0155
B2	2*a*	0.0	0.0	0.8890(5)	0.0155
$Lu_9B_5S_{21}$					
Lu1	6*c*	0.37962(14)	0.15436(14)	0.3142(17)	0.0178(4)
S1	6*c*	0.1358(10)	0.2322(7)	0.4023(18)	0.0173(16)
S2	6*c*	0.1134(8)	0.5382(10)	0.1047(19)	0.0173
S3	2*b*	0.3333	0.6667	0.5650(22)	0.0173
B1	2*b*	0.3333	0.6667	0.239(4)	0.0173
B2	2*a*	0.0	0.0	0.4023(18)	0.0173

three-fold coordinated boron atom was restrained near the barycenter of the sulfur atoms of the $[BS_3]^{3-}$ unit by restraining the distances between boron and sulfur atoms to be 1.85(10) Å and by constraining the z-coordinates of these atoms to be equal. Bond distances between sulfur atoms and boron in tetrahedral coordination were restrained to be 1.90(5) Å. The isotropic displacement parameters of sulfur and boron were constrained to equal values.

2.4. Electron microscopy

In order to investigate homogeneity areas and phase distribution within the reaction products by optical and scanning electron microscopy (SEM), the samples were prepared for metallographic studies by polishing with different polishing disks and micron sized diamond powders (0.25 mm) using dried hexane as a lubricant. Scanning electron microscopy and the determination of the chemical composition of the samples by energy dispersive X-ray spectroscopy (EDXS) were performed using a SEM Philips XL 30 (LaB_6-cathode, accelerating voltage: 25.0 kV, Magnification: 1000 ×) with integrated energy dispersive spectrometer. The EDXS data confirmed the presence of boron and the molar ratios RE:S of 3:7.

Samples for transmission electron microscopy (TEM) were prepared by means of grinding and deposition on a holy-carbon film supported by a copper grid which allowed for TEM investigations using a TECNAI 10 Electron Microscope equipped with a CCD camera.

2.5. X-ray absorption spectroscopy (XAS)

Lu L_{III} X-ray absorption spectra (XAS) of polycrystalline $Lu_9B_5S_{21}$ were recorded in transmission arrangement at the EXAFS beamline C of HASYLAB at DESY. A polyethylene pellet (diameter: 10 mm) containing 18 mg of powdered sample was enclosed in Kapton foil. An Oxford He gas-flow cryostat was used for low temperature measurements at 5 and 100 K, respectively. Measurements were also done at 298 K. Wavelength selection was realized by means of a Si(111) double crystal monochromator which yields an experimental resolution of approximately 0.5 eV (FWHM) for the experimental setup at the Lu L_{III} threshold of 9244 eV. An EXAFS program with initial step size and sample time of ΔE=0.5 eV and t=0.5 s was applied for energies up to 1 keV above the Lu L_{III} edge. For energy calibration Yb_2O_3 was chosen as external reference compound. EXAFS data analysis was performed using the ATHENA and ARTEMIS packages [22]. The EXAFS interference function, $\chi(k)$, was extracted from the measured absorption spectra using the standard procedure [23], which includes pre- and post-edge background removal. The extracted EXAFS signal was weighted by k^2 and Fourier transformed to real space (R) by using the Hanning window function from 2 to ~14 Å^{-1}. Radial distributions, $\varphi(R)$, from 1 to 6 Å around the X-ray absorbing atom were derived. The radial distribution was phase-shift corrected for the description of the position of the S1 atoms within the $[\square(S^{2-})_3]$ substructure, using the 1 × 1 × 3 superstructure model as used for electronic structure calculations for EXAFS data analysis. During the first-principles calculations the coordination numbers were fixed at values indicated by the structural model. One E_0 shift was allowed for the seven sulfur atoms within the first shell (E_0^S (eV): 5.67 ± 0.31) and one for the two boron atoms within the second shell (E_0^B (eV): 4.83 ± 0.46).

2.6. Computational methods

Electronic structure calculations were performed with the all-electron full-potential local orbital (FPLO) method [24]. Local

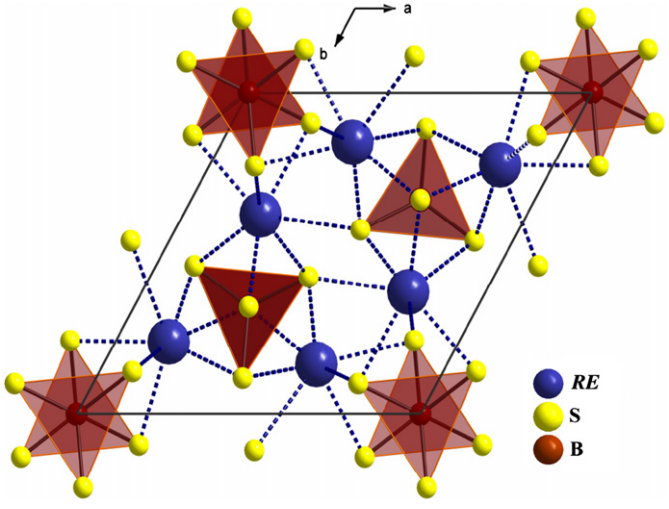

Fig. 2. Crystal structure of $RE_9B_5S_{21}$, (RE=Dy–Lu), viewed along [001].

density approximation to the density functional theory with Perdew–Wang [25] parameterization for the exchange-correlation potential was used. In order to understand the nature of the boron vacancies, 1×1×3 super cells of $Lu_9B_5S_{21}$ were modeled for total energy, force, charge transfer and chemical bonding investigations. All possible vacancy arrangements with vacancies either at the B1 (2*b*) or at the B2 (2*a*) positions (a total of six different models) were considered. A charge transfer analysis was based on Bader's quantum theory of atoms in molecules (QTAIM) [26], while chemical bonding was studied using the concept of electron localizability indicator (ELI) [27]. The latter was computed by a module implemented in version 5 of FPLO [28], and the Basin program [29] was used for the topological analysis. The accuracy of charge transfer analysis was about 0.2 electrons, while the estimated error in electron counts of the chemical bonding analysis was about ±0.03.

3. Results and discussion

Application of Hp–HT conditions yielded samples of the isotypic compounds $RE_9B_5S_{21}$, (*RE*=Dy–Lu) suitable for refinement of the crystal structures from X-ray powder diffraction data (Table 1). The title compounds adopt the $Ce_6Al_{3.33}S_{14}$ structure type [12] (hexagonal, space group $P6_3$, No. 173). Thus, the crystal structures of $RE_9B_5S_{21}$ are closely related to the large family of compounds of general formula $RE_3MM'Q_7$, where *M* and *M*′ are metals or metalloids and *Q* is a chalcogen [30]. However, in the case of the title compounds *M* and *M*′ stand for a non-metallic element, namely boron.

The boron atoms occupy two sites (2*b* and 2*a*) with tetrahedral and trigonal planar coordination by sulfur, respectively (Table 2, Figs. 2 and 3). Isolated $[BS_4]^{5-}$ tetrahedra (all pointing in the polar [001] direction) represent a unique feature of the crystal structure which is observed for the first time in a thioborate compound. The tetrahedra are stacked along the three-fold rotation axes. B1–S2 bond lengths are in the range 1.918–1.947 Å, and B1–S3 in the range 1.922–1.999 Å (Table 3). These values are in agreement with B–S bonds found in other thioborates with four-fold coordinated boron: 1.61–2.06 Å; mean value 1.92(4) Å [31]. The S–B1–S angles are close to the ideal tetrahedral value of 109.5° in all the six compounds. However, in case of *RE*=Er the angle S2–B1–S2 is larger than S2–B1–S3, while it is just the opposite situation in the other five compounds (this disagreement

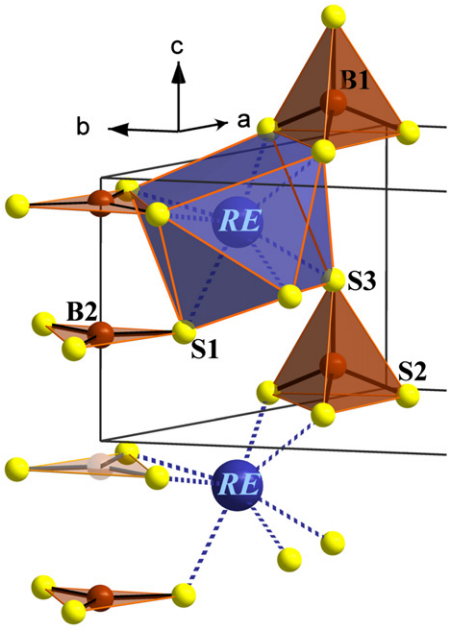

Fig. 3. Detail of the crystal structure of $RE_9B_5S_{21}$, (*RE*=Dy–Lu), showing the stacking of $[BS_4]^{5-}$ tetrahedra and $[BS_3]^{3-}$ triangles propagating along the 6_3 axes and interconnected by RES_{6+1} mono-capped trigonal prisms.

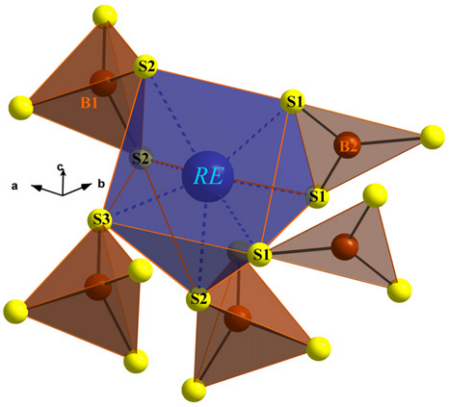

Fig. 4. Detail of the crystal structure of $RE_9B_5S_{21}$, (*RE*=Dy–Lu), showing the coordination polyhedron (mono-capped trigonal prism) around *RE* by two $[BS_3]^{3-}$ and three $[BS_4]^{5-}$ units.

Table 3
Interatomic distances (*d*, Å) within the coordination polyhedra around the *RE* cations as well as bond lengths (Å) and angles (deg) within $[BS_3]^{3-}$ and $[BS_4]^{5-}$ complex ions in the crystal structures of $RE_9B_5S_{21}$, (*RE*=Dy–Lu).

$Dy_9B_5S_{21}$		$Ho_9B_5S_{21}$		$Er_9B_5S_{21}$		$Tm_9B_5S_{21}$		$Yb_9B_5S_{21}$		$Lu_9B_5S_{21}$	
Atoms	*d*(angle)	Atoms	*d*(angle)	Atoms	*d*(angle)	Atoms	*d*(angle)	Atoms	*d*(angle)	Atoms	*d*(angle)
Dy–S2	2.694(9)	Ho–S2	2.692(6)	Er–S1	2.666(13)	Tm–S2	2.684(6)	Yb–S2	2.671(3)	Lu–S2	2.645(9)
Dy–S1	2.725(14)	Ho–S1	2.698(6)	Er–S2	2.679(13)	Tm–S1	2.697(6)	Yb–S1	2.686(4)	Lu–S1	2.692(9)
Dy–S1	2.757(15)	Ho–S1	2.768(6)	Er–S2	2.706(13)	Tm–S1	2.721(5)	Yb–S1	2.712(3)	Lu–S1	2.699(7)
Dy–S1	2.773(11)	Ho–S1	2.790(5)	Er–S1	2.757(13)	Tm–S1	2.743(6)	Yb–S1	2.742(4)	Lu–S1	2.728(9)
Dy–S3	2.796(6)	Ho–S3	2.794(4)	Er–S1	2.834(12)	Tm–S3	2.766(4)	Yb–S3	2.745(3)	Lu–S3	2.739(6)
Dy–S2	2.848(9)	Ho–S2	2.840(5)	Er–S3	2.932(10)	Tm–S2	2.806(6)	Yb–S2	2.790(3)	Lu–S2	2.762(8)
Dy–S2	2.966(9)	Ho–S2	2.964(5)	Er–S2	2.935(9)	Tm–S2	2.936(4)	Yb–S2	2.930(3)	Lu–S2	2.968(8)
B1–S2	1.943(9)	B1–S2	1.935(6)	B1–S2	1.947(9)	B1–S2	1.946(8)	B1–S2	1.957(6)	B1–S2	1.931(9)
B1–S2	1.944(9)	B1–S2	1.936(6)	B1–S2	1.947(9)	B1–S2	1.946(8)	B1–S2	1.957(6)	B1–S2	1.932(9)
B1–S2	1.943(9)	B1–S2	1.935(6)	B1–S2	1.947(9)	B1–S2	1.946(8)	B1–S2	1.957(6)	B1–S2	1.931(9)
B1–S3	1.947(9)	B1–S3	1.926(12)	B1–S3	1.928(17)	B1–S3	1.933(21)	B1–S3	1.933(14)	B1–S3	1.922(20)
B2–S1	1.913(11)	B2–S1	1.909(3)	B2–S1	1.762(7)	B2–S1	1.878(3)	B2–S1	1.872(3)	B2–S1	1.862(5)
S2–B1–S2	106.8(4)	S2–B1–S2	106.9(4)	S2–B1–S2	111.6(5)	S2–B1–S2	106.4(6)	S2–B1–S2	105.6(4)	S2–B1–S2	104.5(7)
S2–B1–S3	112.0(4)	S2–B1–S3	111.9(4)	S2–B1–S3	107.2(5)	S2–B1–S3	112.4(6)	S2–B1–S3	113.1(4)	S2–B1–S3	114.1(6)
S1–B2–S1	120.0	S1–B2–S1	120.0	S1–B2–S1	120.0	S1–B2–S1	120.0	S1–B2–S1	120.0	S1–B2–S1	120.0

Table 4
Comparison of the total energies of the six possible 1×1×3 supercell models of the crystal structure of $Lu_9B_5S_{21}$ with different vacancy arrangements (for more details see text).

Model	Vacancy arrangement along [001]	Total energy (eV/1×1×3 supercell)	Total energy (meV/atom)
$B1_a$	–B–□–□– –B–B–B–	4.72	67.4
$B1_b$	–□–B–B– –B–□–B–	4.39	62.7
$B1_c$	–□–B–B– –□–B–B–	4.91	70.1
$B2_a$	–B–B–□–□–B–B–	1.37	19.6
$B2_b$	–B–B–□–B–B–□–	0.00	0.00
$B2_c$	–B–B–□–B–□–B–	0.34	4.9

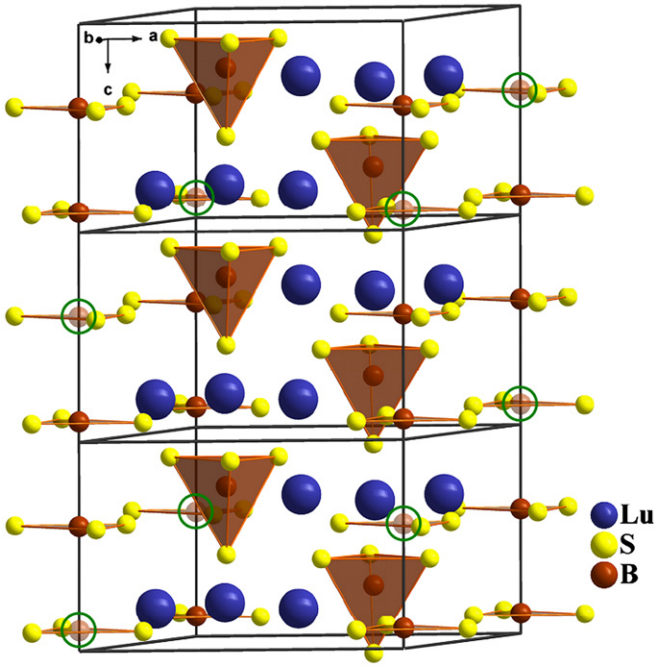

Fig. 5. 1×1×3 supercell model of the crystal structure of $Lu_9B_5S_{21}$ reflecting the most preferred arrangement of boron vacancies. The vacant B2 positions are highlighted with green circles.

is probably due to the quality of powder X-ray diffraction data and the fact that $Er_9B_5S_{21}$ could not be obtained as a single phase sample). By comparing the S2–S2 and S2–S3 interatomic distances within these tetrahedra (3.054–3.4902 and 3.1187–3.8568 Å), it becomes clear that the $[BS_4]^{5-}$ tetrahedra are slightly trigonally elongated. The elongation increases with decreasing size of the *RE* cation, which can be seen from the general measure of polyhedra distortion (υ (%)=100 $[V_i–V_r]/V_r$) as proposed in [32]. The values of υ are increasing from 6.44% to 8.77% along the *RE* series (*RE*=Dy–Lu). This observation may also explain the trend of the lattice parameters along the series with decreasing *a* and *b* (decreasing size of RE^{3+} ions) and the *c* parameter remaining nearly constant (Fig. S6 in the supporting information). Interestingly, the series of related compounds $RE_3Ge_{1.25}S_7$, (*RE*=Ce–Sm, Gd–Ho) [33] adopting the same structure type shows the same phenomenon. The B2–S1 distances found in the $[BS_3]^{3-}$ triangles which propagate along the 6_3 axis with alternating orientation (1.762–1.913 Å) are in agreement with the B–S bond lengths in other thioborates with three-fold coordinated boron: 1.74–1.96 Å; mean value 1.82(4) Å [31]. Each sulfur atom coordinates to three *RE* cations. Altogether, the S-positions of the $[BS_3]^{3-}$ units as well as those of the $[BS_4]^{5-}$ tetrahedra forming the triangle faces parallel (001) adopt the coordination pattern of the oxygen atoms in the crystal structure of λ-Nd$[BO_3]$ [34]. On the other hand, the sulfur atom located on the three-fold axis rather acts as a monodentate ligand towards the three neighboring *RE* cations.

The *RE* cations are surrounded by two $[BS_3]^{3-}$ and three $[BS_4]^{5-}$ units resulting in an overall 6+1 coordination by sulfur forming a mono-capped trigonal prism. One of the $[BS_3]^{3-}$ units acts as a monodentate ligand, while the other one is in a bidentate function. The three sulfur atoms (S1) coordinating this way form one basal plane of the mono-capped trigonal prisms. The other base is formed by two S2 atoms originating from one $[BS_4]^{5-}$ unit (in a bidentate function) and one S3 atom originating from the other $[BS_4]^{5-}$ unit (coordinating in a monodentate manner). The capping sulfur ligand, S2, originates from the third $[BS_4]^{5-}$ unit (Fig. 4). *RE*–S distances are listed in Table 3.

In compliance with the condition of charge balancing one of the boron sites is only partially occupied. The vacancies in the aristotype structure $Ce_6Al_{3.33}S_{14}$ [12] occur at the octahedrally coordinated Al position (2*a* site). Reflecting this fact on the $RE_9B_5S_{21}$ crystal structure, the vacancies are expected to occur at the trigonal boron site (B2, 2*a*). This expectation is in general accordance to the pressure-coordination rule [35]. Due to the fact that refinements of the boron vacancy arrangements based on the X-ray powder diffraction data did not yield any clear result, first-principles

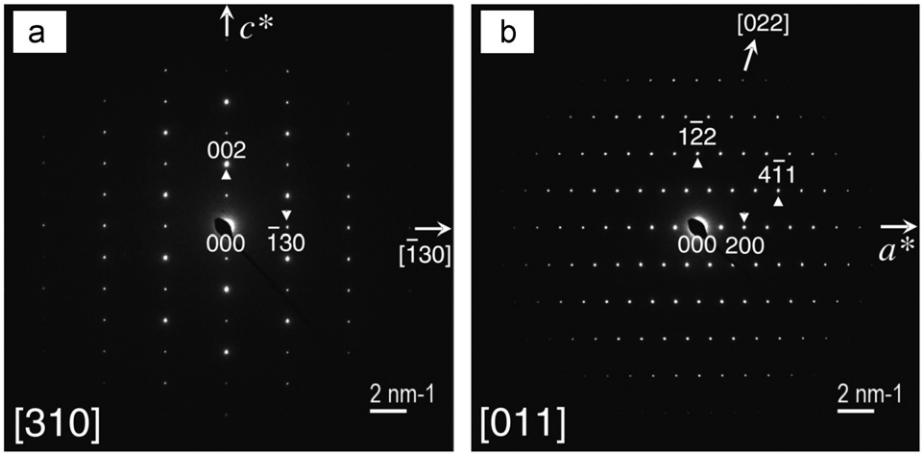

Fig. 6. Selected area electron diffraction (SAED) patterns of $Lu_9B_5S_{21}$ (a) [310] and (b) [011]. No indications for superstructure reflections are observed in the patterns. The forbidden 00*l* reflections with $l=2n+1$ are observed due to dynamical effects.

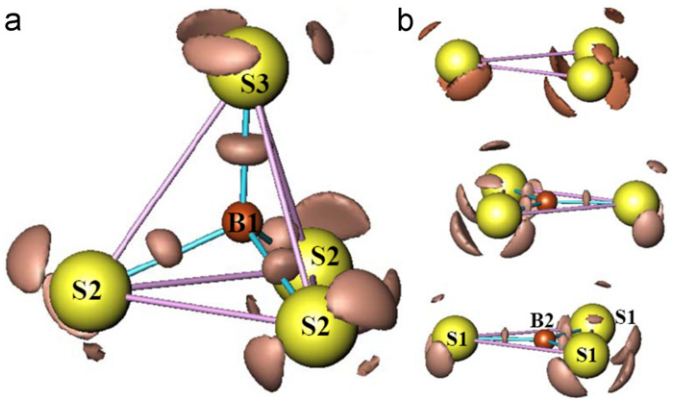

Fig. 7. ELI isosurfaces calculated in the ordered 1×1×3 supercell model of the crystal structure of $Lu_9B_5S_{21}$ showing the valence region ELI attractors for the substructures of interest: (a) $[BS_4]^{5-}$ tetrahedron with isosurface value $Y=1.618$ and (b) $[BS_3]^{3-}$ triangles as well as $[\square(S^{2-})_3]$ arrangements stacked along [001] according to the sequence –B2–B2–□– with isosurface values of $Y=1.628$ and 1.535, respectively, being superimposed. Sulfur atoms are connected by solid lines to indicate the main geometrical objects (S_4 tetrahedron and S_3 triangles).

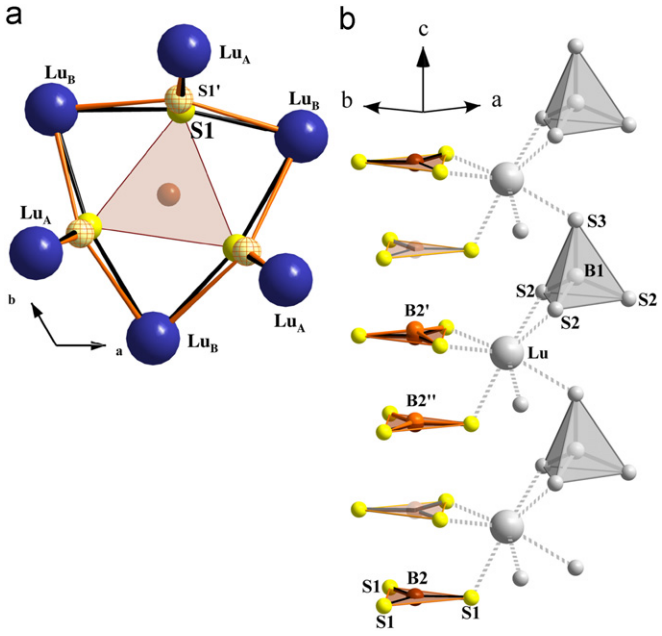

Fig. 8. Illustration of a detail of the crystal structure of $Lu_9B_5S_{21}$ representing FPLO-calculated (a) shifts of the sulfur atoms from the position S1 within the $[BS_3]^{3-}$ unit to position S1' within the $[\square(S^{2-})_3]$ substructure. The brown sphere denotes the B2 site in the $[\square(S^{2-})_3]$ substructure which is unoccupied. (b) shifts of the boron atoms from the position B2 within coplanar $[BS_3]^{3-}$ units to positions B2′ and B2″, both denoted by orange spheres. For further details see text.

calculations were carried out on 1 × 1 × 3 super cells of $Lu_9B_5S_{21}$ in order to model vacancies either at the B1 (2*b*) or the B2 (2*a*) positions (Table 4 and Fig. 5). The electronic structure calculations indicate full occupation of the B1 positions and vacancies are only found at the B2 sites. The lowest total energy was calculated for the model with maximum distances between the Schottky defects, resulting in a preferred –B2–B2–□–B2–B2–□– ordering within the individual [001] columns. Here, every third B2 site is not occupied, and instead a $[\square(S^{2-})_3]$ substructure is formed. Despite ordering within the individual columns, no superstructure is observed as adjacent columns are shuffled by $\pm[00^1/_3]$. That means, shifting up- or downwards is equivalent giving rise to a randomly distributed vacancy pattern of the [001] columns. This vacancy arrangement is most likely induced by minimization of unfavorable Coulomb interactions. Indeed, the electron diffraction patterns of $Lu_9B_5S_{21}$ (Fig. 6) clearly reveal the absence of any superstructure along *c*.

Atomic charges, computed by use of the QTAIM approach for each atom in all six supercell models, show no significant changes depending on which boron site is partially vacant, and how vacancies are ordered. In all cases around 69.1e⁻ belong to Lu atoms, around 17.2e⁻ to S atoms, around 3.6e⁻ to B1 atoms and around 3.4e⁻ to B2 atoms.

The chemical bonding analysis performed on the energetically most favoured 1 × 1 × 3 supercell model, was focused on the three distinct substructures of interest: $[BS_3]^{3-}$, $[BS_4]^{5-}$, and $[\square(S^{2-})_3]$. In Fig. 7 the ELI isosurfaces depicting the relevant chemical bonding situations for a representative of each distinct substructure are shown. The coplanar $[BS_3]^{3-}$ substructure consists of B2 and S1 atoms. The tetrahedral $[BS_4]^{5-}$ unit is composed of B1, one S3 and three S2 atoms, thus there are two types of B–S bonds corresponding to B1–S3 and B1–S2 contacts. The B1–S2 bond is slightly longer than B1–S3 (see Table 3, $Lu_9B_5S_{21}$ column). The B2–S1 bond is the shortest B–S contact being 0.06 Å shorter than B1–S3. All B–S bonds are found to be two-center bonds and the electron counts in the corresponding bond basins are in accordance with the order of the bond lengths. The shortest of all B–S contacts, B2–S1, contains ~2.00e⁻, while B1–S3 contains 1.85e⁻ and the longest one, B1–S2, contains 1.65e⁻. The bonding situation involving the $[BS_3]^{3-}$ units is not affected in any significant way due to optimized B2 atom positions. All the sulfur atoms show three lone-pair-like features with differing electron counts. The 'lone pairs' of the S3 atoms in the $[BS_4]^{5-}$ substructure contain 2.00e⁻ each and obey the symmetry of the three-fold axis, while the lone-pair-like basins of S2 atoms contain 1.93e⁻, 2.05e⁻ and 2.10e⁻. The S1 atoms of the $[BS_3]^{3-}$ substructure contain 1.80e⁻, 1.90e⁻ and 1.92e⁻ in their lone-pair-like basins. The sulfur atoms around the vacant B1 site (the $[\square(S^{2-})_3]$ substructure) show only lone-pair-like features and the interior region of the S_3-triangle does not contain any ELI attractors. The electron counts in the 'lone-pair' basins correspond to 2.0e⁻, 2.6e⁻ and 2.8e⁻, respectively. The bonding topology of the $[BS_3]^{3-}$ substructure is also in agreement with the reported data of gaseous $[BS_3]^{3-}$ ions [36].

The S1 arrangement is of special interest for the structural characterization of the title compounds. Since quantum mechanical calculations indicate vacancies only at the B2 sites, one-third of the S_3 triangles formed by the S1 atoms are empty, viz., $[\square(S^{2-})_3]$. The lack of ELI attractors inside this unit implies that there is no significant covalent bonding among these sulfur atoms that can counterbalance the repulsive Coulomb interactions. Consequently, it is expected that each of the S1 atoms of the $[\square(S^{2-})_3]$ substructure shifts towards the center of the triangle defined by its nearest three *RE* neighbors (*RE*=Dy–Lu), (Fig. 8). The positions of only these S1 atoms (all other atoms were kept fixed) were optimized by using version 9 of the FPLO code. The results are in good agreement with the expectation: S1 atoms of the $[\square(S^{2-})_3]$ substructure indeed move as shown in Fig. 8; the Lu atom above the S_3 plane, denoted as Lu_A, becomes the nearest Lu neighbor of the S1′ atom (bond lengths shortened by ~0.12 Å), while the distances to the other two Lu atoms below (Lu_B) increase very slightly (by ~0.02 and 0.05 Å). In addition, the shortest S1 · · · S1 distance becomes ~0.31 Å longer, so that the effect of Coulomb repulsion is somewhat weakened.

Another interesting feature of the S1 arrangement concerns the question of whether the B2 atoms are coplanar with the S1 atoms or not. Because of the fact that boron is a weak scatterer, it was difficult to answer this question by X-ray diffraction. Therefore, we again turned to first-principles methods. The free *z*-coordinates of the B2 atoms were optimized while keeping all the other atoms fixed. Since along the [001] direction two B2 atoms are sandwiched by two vacancies, cf., –B2–B2–□–B2–B2–□–, it is not clear *a priori*

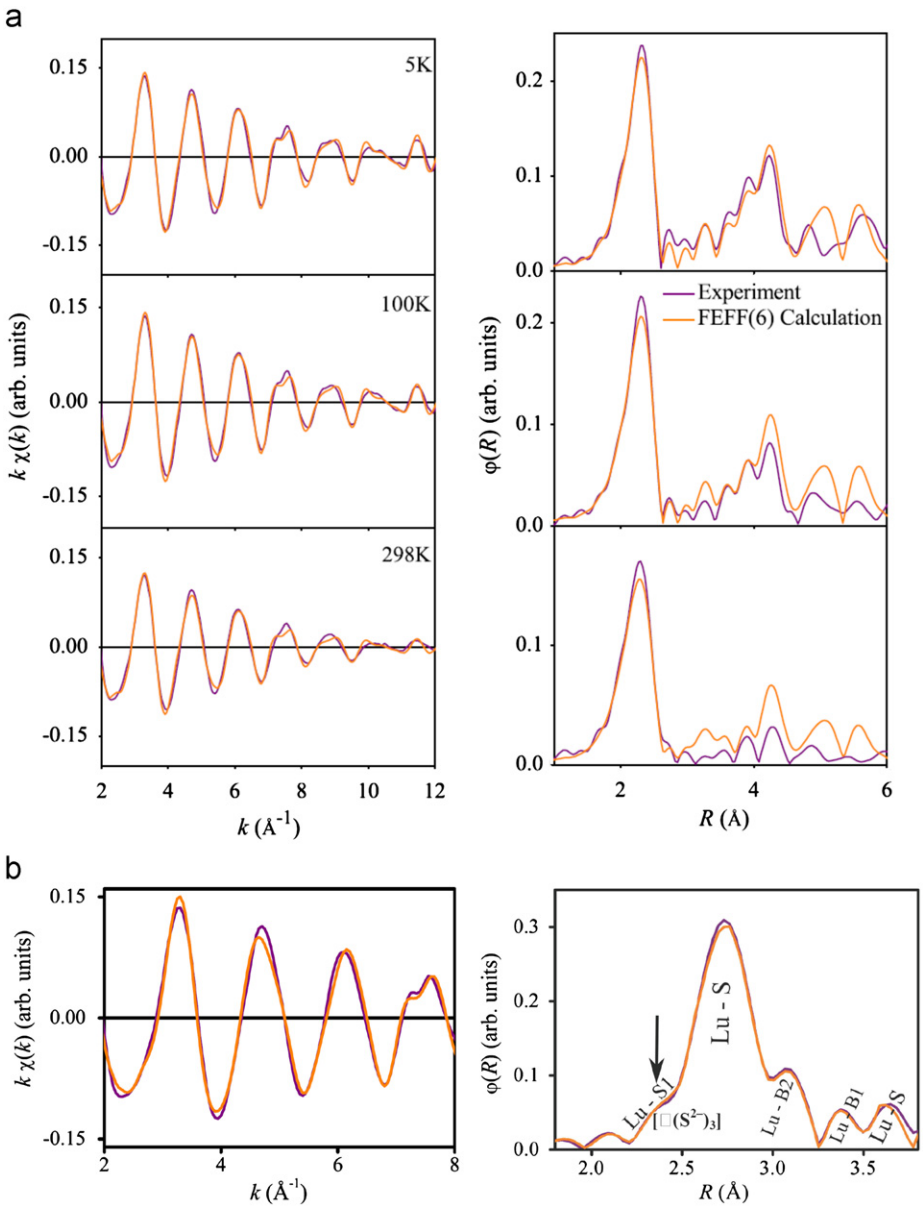

Fig. 9. EXAFS oscillations of $Lu_9B_5S_{21}$ (left) and corresponding Fourier transforms (right) in comparison with the first-principles calculations based on a structure model (a) obtained from the Rietveld refinements and (b) modeled on the base of a $1\times1\times3$ supercell (spectra are phase corrected).

in which direction each boron atom will move, if they move at all. The calculations reflect the absence of a mirror plane perpendicular to the [001] direction. Both boron atoms move away from the S1 layer in the same direction, the one nearest to the vacant site (B2′) in the direction of motion shifts by ~0.217 Å, while the other one (B2″) shifts by about one-third of this value, ~0.065 Å. The direction is determined by the orientation of the $[BS_4]^{5-}$ substructure, pointing from the S2-triangle of the tetrahedron towards the apex atom S3 (Fig. 8b).

The analysis of the EXAFS data confirmed the local structure information around the Lu atoms obtained from X-ray powder diffraction data (Fig. 9a and Table 5). The vacancies are located on the B2 sites in agreement with the quantum mechanical calculations. The detailed analysis of the EXAFS data showed that, using the structural model from the Rietveld refinements, the best fit is obtained for the data taken at low temperature (5 K). At this temperature the ambiguity concerning contributions caused by dynamic or static disorder affecting the EXAFS signal is minimal. The comparison of first-principles calculations [37] assuming vacancies on the B1 site with the experimental data resulted in much higher R values (Table 6). In order to describe the position of the S1 atoms within the $[\square(S^{2-})_3]$ substructure, the analysis of EXAFS data (obtained at 5 K) was best performed using the $1\times1\times3$ superstructure model as already used for electronic structure calculations. The peak originating from the Lu–S bonds has a shoulder at ~2.5 Å, possibly indicating the shift of sulfide ions within the $[\square(S^{2-})_3]$ substructure towards the barycenter of the three coordinated Lu cations (Fig. 9b).

4. Conclusions

The isotypic *RE*–thioborate–sulfides with composition $RE_9B_5S_{21}$, (*RE*=Dy–Lu) were synthesized by means of a high-pressure high-temperature route. The crystal structures were refined from X-ray powder diffraction data, while quantum mechanical calculations revealed information on the arrangement of intrinsic vacancies. The crystal structures are characterized by two types of complex

Table 5
Local structure information around Lu atoms in the crystal structure of $Lu_9B_5S_{21}$, obtained from the analysis of EXAFS oscillations. Overall amplitude factor S_0^2: 0.527; independent points: 53.65, number of variables in fit: 13, *R*-factor; 0.023; χ^2: 847.76, reduced χ^2: 20.86, *k*-space interval: [2: 14.152]; *R*-space interval: [1: 6].

	R (Å) [a]	*R* (Å) [b]	Δ*R* (Å)	σ^2 (10^{-3} Å^2)
Shell 1/CN=7				
Lu–S1	2.728	2.726	0.002	4.1 ± 0.4
Lu–S1	2.692	2.691	0.001	3.8 ± 0.5
Lu–S1	2.699	2.698	0.001	3.8 ± 0.5
Lu–S2	2.645	2.644	0.001	3.6 ± 0.5
Lu–S2	2.968	2.967	0.001	4.6 ± 0.8
Lu–S2	2.762	2.761	0.001	4.2 ± 0.6
Lu–S3	2.739	2.738	0.001	4.2 ± 0.3
Shell 2/CN=2				
Lu – –B1	3.407	3.406	0.001	6.4 ± 0.7
Lu – –B2	3.091	3.089	0.002	5.5 ± 0.4

[a] Distances as expected from refined crystal structure.
[b] Distances obtained from the EXAFS fit using the structural model from the Rietveld refinements.

Table 6
R values of EXAFS fits for $Lu_9B_5S_{21}$ with starting models from the Rietveld refinements (assuming vacancies on B1 and B2 site, respectively) as well as from the $1 \times 1 \times 3$ supercell model with the lowest total energy. For further details see text, Section 3.

Temperature	Assumed vacancy position		
	Model obtained from the Rietveld refinement		Modeled $1 \times 1 \times 3$ superstructure
	B1	B2	B2
	R (%)	*R* (%)	*R* (%)
5 K	9.5	2.3	3.2
100 K	15.7	4.1	–
298 K	30.0	6.7	–

anions: tetrahedral $[BS_4]^{5-}$ and trigonal planar $[BS_3]^{3-}$ as well as $[\square(S^{2-})_3]$ units. Vacancies are located at the trigonal planar coordinated boron site with preferred ordering –B2–B2–□–B2–B2–□– along [001]. No superstructure is observed by means of diffraction methods as adjacent columns are shuffled along the *c*-axis, giving rise to a randomly distributed vacancy pattern. Chemical bonding analysis showed the relevant chemical bonding situations for each of the distinct substructures of interest: $[BS_4]^{5-}$, $[BS_3]^{3-}$ and $[\square(S^{2-})_3]$. In accordance with the combined results of experimental and computational investigations, the chemical formula of the title compounds is consistent with $RE_3[BS_3]_2[BS_4]_3S_3$. Careful optimization of the reaction conditions, namely pressure, temperature and treatment time, as well as the composition of the starting mixtures of elements were needed to obtain this series of thioborate compounds. Further optimizations will be focused on the preparation of *RE* selenoborates.

Supplementary data

Further details of the crystal structure investigations may be obtained from the Fachinformationszentrum Karlsruhe, 76344 Eggenstein-Leopoldshafen, Germany (fax: (+49)7247-808-666; e-mail: crysdata@fiz-karlsruhe.de, http://www.fiz-karlsruhe. de/request_for_deposited_data.html) on quoting the CSD numbers 421967-421972. Rietveld plots, additional figures and tables are presented in the supporting information.

Acknowledgments

The authors gratefully acknowledge Horst Borrmann, Yuri Prots and Steffen Hückmann (X-ray powder diffraction), Petra Scheppan (EDXS), Gudrun Auffermann and Anja Völzke (elemental analysis) as well as Susann Leipe and Katrin Meier for their help with high-pressure high-temperature experiments. The authors are grateful to Prof. Bernt Krebs and Adrienne Hammerschmidt for fruitful discussions. A.O. thanks the IFW Leibniz Institute for Solid State and Materials Research Dresden for computational facilities. The Deutsche Elektronen-Synchrotron facility DESY HASYLAB in Hamburg, Germany, is acknowledged for the beam time to perform XAS measurements.

Appendix A. Supporting information

Supplementary data associated with this article can be found in the online version at doi:10.1016/j.jssc.2010.11.004.

References

[1] B. Krebs, A. Hammerschmidt, M. Döch, Phys. Chem. Glasses 44 (2003) 132–134.
[2] B. Krebs, Angew. Chem. Int. Ed. Engl. 22 (1983) 113–134.
[3] O. Conrad, C. Jansen, B. Krebs, Angew. Chem. Int. Ed. Engl. 37 (1998) 3208–3218.
[4] A. Hammerschmidt, M. Döch, M. Wulff, B. Krebs, Z. Anorg. Allg. Chem. 628 (2002) 2637–2640.
[5] M. Döch, A. Hammerschmidt, B. Krebs, Z. Anorg. Allg. Chem. 630 (2004) 519–522.
[6] J. Hunger, M. Borna, R. Kniep, (2010), La[BS_3], unpublished data.
[7] J. Hunger, M. Borna, R. Kniep, J. Solid State Chem. 182 (2010) 702–706.
[8] J. Hunger, M. Borna, R. Kniep, Z. Kristallogr. NCS 225 (2010) 117–118.
[9] M. Borna, J. Hunger, R. Kniep, Z. Kristallogr. NCS 225 (2010) 223–224.
[10] M. Borna, J. Hunger, R. Kniep, (2010), Gd[BS_3], unpublished data.
[11] M. Borna, J. Hunger, R. Kniep, Z. Kristallogr. NCS 225 (2010) 225–226.
[12] D. de Saint-Giniez, P. Laruelle, J. Flahaut, C.R. Séances, Acad. Sci. Ser. C 267 (1968) 1029–1032.
[13] A. Wosylus, Yu. Prots, U. Burkhardt, W. Schnelle, U. Schwarz, Sci. Technol. Adv. Mater. 8 (5)(2007) 383–388.
[14] D. Walker, M.A. Carpenter, C.M. Hitch, Am. Miner 75 (1990) 1020–1028.
[15] D.A. Young, Phase Diagrams of the Elements, UC Press, 1991.
[16] A.L. Bail, Powder Diffr. 19 (3)(2004) 249–254.
[17] L.G. Akselrud, P.Y. Zavalii, Yu.N. Grin, V.K. Pecharsky, B. Baumgartner, E. Wölfel, Mater. Sci. Forum 133–136 (1993) 335–340.
[18] V. Favre-Nicolin, R. Černý, J. Appl. Crystallogr. 35 (2002) 734–743.
[19] H.M. Rietveld, J. Appl. Crystallogr. 2 (1969) 65–71.
[20] A. Larson, R.V. Dreele, General structure analysis system (GSAS), Los Alamos National Library Report LAUR 86–748.
[21] B.H. Toby, J. Appl. Crystallogr. 34 (2001) 210–213.
[22] B. Ravel., M. Newville, J. Synchrotron Radiat. 12 (2005) 537–541.
[23] H. Maeda, J. Phys. Soc. Jpn. 56 (1987) 2777–2787.
[24] K. Koepernik, H. Eschrig, Phys. Rev. B 59 (1999) 1743–1757 〈www.fplo.de〉.
[25] J.P. Perdew, Y. Wang, Phys. Rev. B 45 (1992) 13244–13249.
[26] R.F.W. Bader, Atoms in Molecules – A Quantum Theory, Clarendon Press, Oxford, 1990.
[27] M. Kohout, Int. J. Quantum Chem. 97 (2004) 651–658.
[28] A. Ormeci, H. Rosner, F.R. Wagner, M. Kohout, Yu. Grin, J. Phys. Chem. A 110 (2006) 1100–1105.
[29] M. Kohout, Program Basin, version 4.2, MPI Chemical Physics of Solids, Dresden (2007).
[30] P. Villars, Pearson's Handbook, Desk Edition, Materials Park, Ohio, 1997.
[31] Inorganic crystal structure database, version 2009/01; http://www.fiz-karlsruhe.de/icsd_home.html.
[32] E. Makovicky, T. Balic-Zunic, Acta Crystallogr. B 54 (1998) 766–773.
[33] A. Michelet, A. Mazurier, G. Collin, P. Laruelle, J. Flahaut, J. Solid State Chem. 13 (1975) 65–76.
[34] H. Müller-Bunz, T. Nikelski, T. Schleid, Z. Naturforsch. 58b (2003) 375–380.
[35] A. Neuhaus, Chimia 18 (1964) 93–103.
[36] T. Takaluoma, T. Säkkinen, T. Bajorek, R. Laitinen, B. Krebs, H. Conrad, O. Conrad, J. Mol., Struct. Theochem 821 (2007) 1–8.
[37] S.I. Zabinsky, J.J. Rehr, A. Ankudinov, R.C. Albers, M.J. Eller, Phys. Rev. B 52 (1995) 2995–3009.